Arch Appl Mech 87:927–947
DOI 10.1007/s00419-016-1223-8

ORIGINAL

**H. Yazdani Sarvestani** · **A. H. Akbarzadeh**

# Thick isotropic curved tubes: three-dimensional stress analysis

Received: 7 August 2015 / Accepted: 20 December 2016 / Published online: 4 January 2017


**Abstract** While the structural analysis of straight beams is straightforward, the behavior of curved beams is more complex to predict. In the present work, a displacement approach of toroidal elasticity is used to analyze thick isotropic curved tubes subjected to axial load, torque, and bending moment. The governing equations are developed in a toroidal coordinate. The method of successive approximation is used to obtain the general solution. The accuracy of the present methodology is tested comparing the numerical results with those obtained by finite element method (FEM) and stress-based toroidal elasticity (SBTE). The proposed methodology is computationally cost-effective, and its results reveal good agreements with FEM and SBTE results. Finally, several numerical examples of stress distributions in thick isotropic curved tubes under axial load, torque, and bending moment are presented. By using the present methodology, displacements as well as stresses are obtained which are important information for fracture analysis.

**Keywords** Thick curved tubes · Toroidal elasticity · Displacement-based solution · Successive approximation · Mechanical load

## List of symbols

| | |
|---|---|
| $a, b$ | Inside and outside cross-sectional radius of the curved tube |
| $c$ | Reference length |
| $a_n, b_n, c_n, d_n, e_n, f_n$ | Constants of the $n$th-order complementary solution |
| $A_{ni}, B_{ni}, C_{ni}$ | Constants of the $n$th-order particular solution |
| $E$ | Young's modulus |
| $G$ | Shear's modulus |
| $F_z, T_z, M_y$ | Axial load, torque and bending moment |
| $R$ | Mean radius of an isotropic curved tube |
| $u_\varsigma, u_\phi, u_\theta$ | Displacement components in toroidal coordinates |
| $u, v, w$ | Non-dimensional displacement components |
| $u_k, v_k, w_k$ | The $k$th-order non-dimensional displacement components |
| $U, V, W$ | The first part of Navier function |
| $\bar{U}, \bar{V}, \bar{W}$ | The second part of Navier function |
| $\hat{U}, \hat{V}, \hat{W}$ | The third part of Navier function |

H. Yazdani Sarvestani (✉) · A. H. Akbarzadeh (✉)
Department of Bioresource Engineering, McGill University, Montreal, QC H9X 3V9, Canada
E-mail: hamidreza.yazdani@mail.mcgill.ca

A. H. Akbarzadeh
E-mail: hamid.akbarzadeh@mcgill.ca

| | |
|---|---|
| $U_k, V_k, W_k$ | The first part of Navier function of the $k$th order |
| $\bar{U}_k, \bar{V}_k, \bar{W}_k$ | The second part of Navier function of the $k$th order |
| $\hat{U}_k, \hat{V}_k, \hat{W}_k$ | The third part of Navier function of the $k$th order |
| $\varepsilon$ | $a/R$ |
| $\upsilon$ | Poisson's ratio |
| $\varsigma, \phi, \theta$ | Toroidal coordinates |
| $\tau_{\varsigma\varsigma}, \tau_{\phi\phi}, \tau_{\theta\theta}$ | Non-dimensional normal stress components |
| $\tau_{\varsigma\phi}, \tau_{\phi\theta}, \tau_{\varsigma\theta}$ | Non-dimensional shear stress components |
| $\tau_{\varsigma\varsigma k}, \tau_{\phi\phi k}, \tau_{\theta\theta k}$ | The $k$th-order non-dimensional normal stress components |
| $\tau_{\varsigma\phi k}, \tau_{\phi\theta k}, \tau_{\varsigma\theta k}$ | The $k$th-order non-dimensional shear stress components |

## 1 Introduction

The stress analysis of curved structures is often theoretically and computationally complex. Governing equations of curved structures are much more complicated than straight structural elements [1,2]. The curve-like structures exhibit complex deformation fields given their toroidal geometry and the multiplicity of external load configurations. One type of the curve-like structures is isotropic curved tubes used in pressure vessel industries, chemical reactors, steam generators and rotational gas compressor applications.

Von Karman [3] found a theoretical explanation to justify how a curved tube could have a higher bending flexibility than a straight beam. The particular case of this problem, so-called Brazier effect, including the buckling analysis of straight or curved tubes was found complex to be analyzed [4]. The research works of Von Karman and Brazier provided basis for the subsequent analysis of tube problems. Ting [5,6] and Chen et al. [7] investigated stress analysis in an anisotropic cylindrical tube under pressure, shear, torsion and tensile loads. Boyle [8] used nonlinear shell theory shell to formulate the tube bending problem. Reissner [9] presented a finite bending theory for curved tubes. Emmerling [10] determined the nonlinear deformation of elastic curved tubes subjected to bending. In addition, he studied the precritical deformation of tubes on the basis of a semi-membrane theory. The semi-membrane theory is free of drawbacks of the membrane theory such as inapplicability of stress analysis of long cylindrical shells and impossibility of satisfying prescribed boundary conditions on the longitudinal edges of open cylindrical shells.

The theory of toroidal elasticity (TE) has been employed to determine stress and displacement fields in toroidal rings and vessels utilized in chemical and power plants under different types of loads [11]. Gohner [12] apparently was the first researcher to report the technical complexity of the analysis of a curved solid circular ring sector subjected to pure twist and bending moments. Ancker and Goodier [13] investigated helical springs subjected to tension and torsional loads using the thin-slice method. They assumed that the springs had the same cross section and same resultant force and moments at each cross section of spring. Kornecki [14] and McGill [15] developed the TE theory extending Gohner's research work. Kornecki [14] employed the method of successive approximation to solve the governing equations, while the finite difference method was applied by McGill [15]. Major contribution to the TE theory was from Lang [11]. Lang summarized prior research works [11] and developed a new TE theory in toroidal coordinate system. In the aforementioned Lang's research, the stress function approach has been employed; as a result, the deformation fields have not been derived directly. Redekop [16,17] used the displacement components as basic variables and developed governing Navier equations in toroidal coordinate system. Eric [18] investigated the linear problem of pure bending of thin curved tubes. The solution of a circular cylindrical shell under a uniform pressure was employed as the first approximation for the solution of the bending problem. A solution was obtained for the stress intensity factor of double-curvature tubes close to the cracked area [19]. A numerical solution was proposed by Fonseca and Melo [20] to perform a stress analysis of curved tubes under in-plane bending forces. Kolesnikov [21] considered a short sector of torus as a curved tube and analyzed its large pure bending deformations. Mathematical equations were presented to study effects of tube thickness on the collapse loads in the curved tubes under in-plane bending moment. The comparison was made using finite element to verify the proposed equations [22]. Zhu et al. [23] investigated the finite deformation of a thick elastic tube under internal or external pressure and zero displacement on its ends using a Galerkin method combined with a Newton iteration solver. Levyakov [24] studied nonlinear equations of in-plane bending of curved tubes based on Reissner's formulation in terms of two unknown functions and parameters. To solve the equations, a numerical method based on finite difference approximations and Newton–Raphson iteration technique was developed. The buckling of a straight tube subjected to a pure bending moment was also studied by nonlinear the finite element method (FEM) [25],

and the effects of imperfections on the buckling of thick curved panels were studied [26]. The deformation of a circular cylindrical tube of a homogeneous transversely isotropic elastic material subjected to axial load, internal pressure and end support moments was analyzed. Mathematical formulas were presented for the resultant axial load and torsional moment at the ends of the tube a based on general strain energy function [27]. Recently, Djamaluddin et al. [28] implemented a finite element analysis to investigate the dynamic response of tubes for axial progressive and global bending. Finally, Rodríguez and Merodio [29] investigated the torsion of a tube subjected to radial and circumferential residual stresses. The developed numerical method was able to capture the elastic instability of tubes under torque.

Considering the mesh sensitivity and computational costs of finite element approach, it is desired to develop an analytical or semi-analytical method for stress analysis of complex curve-like structures. The present paper studies theoretically stresses developed within thick isotropic curved tubes under axial load, torque and bending moment. The displacement-based toroidal elasticity (DBTE) including a full three-dimensional constitutive relation is used for the analysis. Numerical results are compared with those developed analytically using SBTE and numerically using FEM via ANSYS software. The three-dimensional stress distribution within thick isotropic curved tubes is presented for a series of load case scenarios.

## 2 Displacement-based toroidal elasticity (governing equations)

A thick isotropic curved tube with a bending radius $R$ and an annular cross section bounded by radii $a$ and $b$ is subjected to axial load $F_z$, torque $T_z$ and bending moment $M_y$, in the plane of the curved tube as shown in Fig. 1. A general point $P$ in a constant thickness curved tube can be represented easily by toroidal coordinate system ($r$, $\Phi$ and $\theta$) where $r$ and $\Phi$ are polar coordinates in the plane of the tube cross section and $\theta$ defines the position of the curved tube cross section as seen in Fig. 2. A non-dimensional radial coordinate ($\varsigma = r/c$) is defined in the toroidal coordinate which $c$ is a reference length to be determined later. Non-dimensional displacements $u$, $v$ and $w$ are defined as:

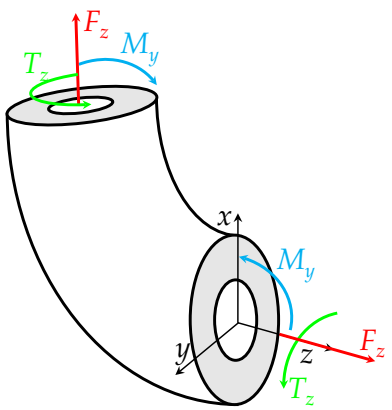


**Fig. 1** Mechanical loadings acting on the isotropic curved tube

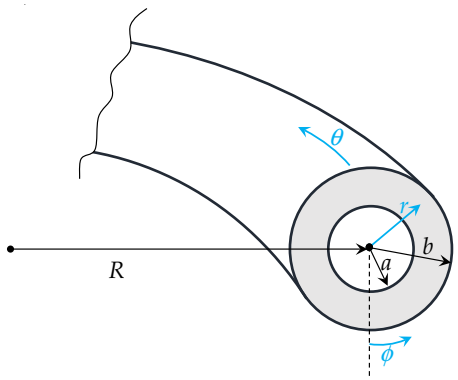


**Fig. 2** Geometry and coordinate system of the curved tube

$$u = \frac{u_\varsigma}{c}, \quad v = \frac{u_\phi}{c}, \quad w = \frac{u_\theta}{c} \tag{1}$$

Non-dimensional stress components are defined as [16]:

$$\begin{aligned} \tau_{\varsigma\varsigma} &= \frac{1+\upsilon}{E}\sigma_{\varsigma\varsigma}, \quad \tau_{\phi\phi} = \frac{1+\upsilon}{E}\sigma_{\phi\phi}, \quad \tau_{\theta\theta} = \frac{1+\upsilon}{E}\sigma_{\theta\theta} \\ \tau_{\varsigma\phi} &= \frac{1+\upsilon}{E}\sigma_{\varsigma\phi}, \quad \tau_{\varsigma\theta} = \frac{1+\upsilon}{E}\sigma_{\varsigma\theta}, \quad \tau_{\phi\theta} = \frac{1+\upsilon}{E}\sigma_{\phi\theta} \end{aligned} \tag{2}$$

The kinematics relations are:

$$\begin{aligned} \varepsilon_{\varsigma\varsigma} &= \tfrac{\partial u}{\partial \varsigma}, & \varepsilon_{\varsigma\phi} &= \tfrac{1}{2}\left(\tfrac{1}{\varsigma}\tfrac{\partial u}{\partial \phi} + \tfrac{\partial v}{\partial \varsigma} - \tfrac{v}{\varsigma}\right), \\ \varepsilon_{\phi\phi} &= \tfrac{u}{\varsigma} + \tfrac{1}{\varsigma}\tfrac{\partial v}{\partial \phi}, & \varepsilon_{\varsigma\theta} &= \tfrac{1}{2}\left(\tfrac{\partial w}{\partial \varsigma} + \tfrac{1}{\rho}\tfrac{\partial u}{\partial \theta} - \tfrac{w}{\rho}\cos\phi\right), \\ \varepsilon_{\theta\theta} &= \tfrac{1}{\rho}\left(u\cos\phi - v\sin\phi + \tfrac{\partial w}{\partial \theta}\right), & \varepsilon_{\phi\theta} &= \tfrac{1}{2}\left(\tfrac{1}{\varsigma}\tfrac{\partial w}{\partial \phi} + \tfrac{1}{\rho}\tfrac{\partial v}{\partial \theta} + \tfrac{w}{\rho}\sin\phi\right) \end{aligned} \tag{3}$$

where $\rho = R + \mathrm{rcos}\Phi$ is the radial cylindrical coordinate of a general point. The non-dimensional stress components are presented in terms of three non-dimensional displacement components as:

$$\begin{aligned} \tau_{\varsigma\varsigma} &= \tfrac{\partial u}{\partial \varsigma} + \tfrac{\nu}{1-2\nu}\vartheta, & \tau_{\varsigma\phi} &= \tfrac{1}{2}\left(\tfrac{1}{\varsigma}\tfrac{\partial u}{\partial \phi} + \tfrac{\partial v}{\partial \varsigma} - \tfrac{v}{\varsigma}\right) \\ \tau_{\phi\phi} &= \left(\tfrac{u}{\varsigma} + \tfrac{1}{\varsigma}\tfrac{\partial v}{\partial \phi}\right) + \tfrac{\nu}{1-2\nu}\vartheta, & \tau_{\varsigma\theta} &= \tfrac{1}{2}\left(\tfrac{\partial w}{\partial \varsigma} + \tfrac{c}{\rho}\tfrac{\partial u}{\partial \theta} - \tfrac{c}{\rho}w\cos\phi\right) \\ \tau_{\theta\theta} &= \tfrac{c}{\rho}\chi + \tfrac{\nu}{1-2\nu}\vartheta, & \tau_{\phi\theta} &= \tfrac{1}{2}\left(\tfrac{1}{\varsigma}\tfrac{\partial w}{\partial \phi} + \tfrac{c}{\rho}\tfrac{\partial v}{\partial \theta} + \tfrac{c}{\rho}w\sin\phi\right) \end{aligned} \tag{4}$$

where

$$\vartheta = \psi + \frac{c}{\rho}\chi, \quad \psi = \frac{\partial u}{\partial \varsigma} + \frac{u}{\varsigma} + \frac{1}{\varsigma}\frac{\partial v}{\partial \phi}, \quad \chi = u\cos\phi - v\sin\phi + \frac{\partial w}{\partial \theta} \tag{5}$$

Three equilibrium equations in the stress form in the toroidal coordinate are represented as [17]:

$$\begin{aligned} &\frac{\partial \tau_{\varsigma\varsigma}}{\partial \varsigma} + \frac{1}{\varsigma}\frac{\partial \tau_{\varsigma\phi}}{\partial \phi} + \frac{1}{\varsigma}\left(\tau_{\varsigma\varsigma} - \tau_{\phi\phi}\right) + \frac{c}{\rho}\left(\frac{\partial \tau_{\varsigma\theta}}{\partial \theta} + \left(\tau_{\varsigma\varsigma} - \tau_{\phi\phi}\right)\cos\phi - \tau_{\varsigma\phi}\sin\phi\right) = 0 \\ &\frac{\partial \tau_{\varsigma\phi}}{\partial \varsigma} + \frac{1}{\varsigma}\frac{\partial \tau_{\phi\phi}}{\partial \phi} + \frac{2}{\varsigma}\tau_{\varsigma\phi} + \frac{c}{\rho}\left(\frac{\partial \tau_{\phi\theta}}{\partial \theta} + \tau_{\varsigma\phi}\cos\phi - \left(\tau_{\phi\phi} - \tau_{\theta\theta}\right)\sin\phi\right) = 0 \\ &\frac{\partial \tau_{\varsigma\theta}}{\partial \varsigma} + \frac{1}{\varsigma}\frac{\partial \tau_{\phi\theta}}{\partial \phi} + \frac{1}{\varsigma}\tau_{\varsigma\theta} + \frac{c}{\rho}\left(\frac{\partial \tau_{\theta\theta}}{\partial \theta} + 2\tau_{\varsigma\theta}\cos\phi - 2\tau_{\phi\theta}\sin\phi\right) = 0 \end{aligned} \tag{6}$$

Substituting the stress-displacement relations [Eq. (4)] into the equilibrium equations [Eq. (6)], the governing Navier equations in the toroidal coordinate system are obtained as:

$$\begin{aligned} U + \left(\frac{c}{\rho}\right)^1 \bar{U} + \left(\frac{c}{\rho}\right)^2 \hat{U} = 0 \\ V + \left(\frac{c}{\rho}\right)^1 \bar{V} + \left(\frac{c}{\rho}\right)^2 \hat{V} = 0 \\ W + \left(\frac{c}{\rho}\right)^1 \bar{W} + \left(\frac{c}{\rho}\right)^2 \hat{W} = 0 \end{aligned} \tag{7}$$

where the coefficients in Eq. (7) are defined in "Appendix 1." Three Navier equations serve as fundamental equations for DBTE. These equations are composed of three parts. The first part is independent of $c/\rho$. The second and the third parts are the linear and nonlinear parts of $c/\rho$, respectively. Navier equations in the toroidal coordinate system are much more complicated than those in the Cartesian coordinate system. As it is impossible to find an exact solution for the presented Navier equations, the method of successive approximation [16] is used to develop an approximate numerical solution. We should note that tubes are considered thick when the geometry of a curved tube has the condition of $2(b-a)/(b+a) > 0.1$. As a result, the proposed method could be applied for this geometry condition to calculate stresses accurately; otherwise, shell theories may be used to obtain stresses in thin and moderately thick curved tubes.

## 3 Method of successive approximation

The method of successive approximation is employed to solve Navier equations in the toroidal coordinate system. The solution for each displacement component is assumed to be in the form of series in terms of a small parameter $\varepsilon$. The parameter $\varepsilon$ is chosen as:

$$\varepsilon = \frac{c}{R} \tag{8}$$

Therefore, the non-dimensional displacement components can be written as:

$$\begin{aligned} u &= \sum \varepsilon^n u_n \\ v &= \sum \varepsilon^n v_n \\ w &= \sum \varepsilon^n w_n \quad n = 0, 1, 2, 3, \ldots \end{aligned} \tag{9}$$

where $n$ indicates the order of the displacement components in the series. Substituting the series form displacement functions [Eq. (9)] into Eq. (4), the corresponding non-dimensional stress components are obtained:

$$\begin{array}{llll} \tau_{\varsigma\varsigma} = \sum \varepsilon^n \tau_{\varsigma\varsigma n} & \tau_{\varsigma\phi} = \sum \varepsilon^n \tau_{\varsigma\phi n} & & \\ \tau_{\phi\phi} = \sum \varepsilon^n \tau_{\phi\phi n} & \tau_{\varsigma\theta} = \sum \varepsilon^n \tau_{\varsigma\theta n} & & \\ \tau_{\theta\theta} = \sum \varepsilon^n \tau_{\theta\theta n} & \tau_{\phi\theta} = \sum \varepsilon^n \tau_{\phi\theta n} & n = 0, 1, 2, 3, \ldots & \end{array} \tag{10}$$

The functions of Navier equations are expanded in the following form:

$$\begin{array}{lllll} U = \sum \varepsilon^n U_n & V = \sum \varepsilon^n V_n & W = \sum \varepsilon^n W_n & & \\ \bar{U} = \sum \varepsilon^n \bar{U}_n & \bar{V} = \sum \varepsilon^n \bar{V}_n & \bar{W} = \sum \varepsilon^n \bar{W}_n & & \\ \hat{U} = \sum \varepsilon^n \hat{U}_n & \hat{V} = \sum \varepsilon^n \hat{V}_n & \hat{W} = \sum \varepsilon^n \hat{W}_n & n = 0, 1, 2, 3, \ldots & \end{array} \tag{11}$$

The quantities $c/\rho$ and $(c/\rho)^2$ are developed in the form of series of the parameter $\varepsilon$ using Taylor Theorem as:

$$\begin{aligned} \frac{c}{\rho} &= \varepsilon - \varepsilon^2 \varsigma^2 \cos\phi + \varepsilon^3 \varsigma^3 \cos^2\phi - \cdots \\ \left(\frac{c}{\rho}\right)^2 &= \varepsilon^2 - 2\varepsilon^3 \varsigma \cos\phi + 3\varepsilon^4 \varsigma^2 \cos^2\phi - \cdots \end{aligned} \tag{12}$$

Substituting the expanded Navier functions and Eq. (12) into Navier equations [Eq. (7)], matching terms with the same order of $\varepsilon$, and setting each corresponding factors with the same order of $\varepsilon$ to zero, the governing equations for the different orders are derived. The equations are indicated for *the zeroth order* as:

$$U_0 = 0, \quad V_0 = 0, \quad W_0 = 0 \tag{13}$$

For the first order as:

$$U_1 = -\bar{U}_0, \quad V_1 = -\bar{V}_0, \quad W_1 = -\bar{W}_0 \tag{14}$$

For the second order as:

$$\begin{aligned} U_2 &= -\bar{U}_1 + \bar{U}_0 \varsigma \cos\phi - \hat{U}_0 \\ V_2 &= -\bar{V}_1 + \bar{V}_0 \varsigma \cos\phi - \hat{V}_0 \\ W_2 &= -\bar{W}_1 + \bar{W}_0 \varsigma \cos\phi - \hat{W}_0 \end{aligned} \tag{15}$$

For the third order as:

$$\begin{aligned} U_3 &= -\bar{U}_2 + \bar{U}_1 \varsigma \cos\phi - \bar{U}_0 \varsigma^2 \cos^2\phi - \hat{U}_1 + 2\hat{U}_0 \varsigma \cos\phi \\ V_3 &= -\bar{V}_2 + \bar{V}_1 \varsigma \cos\phi - \bar{V}_0 \varsigma^2 \cos^2\phi - \hat{V}_1 + 2\hat{V}_0 \varsigma \cos\phi \\ W_3 &= -\bar{W}_2 + \bar{W}_1 \varsigma \cos\phi - \bar{W}_0 \varsigma^2 \cos^2\phi - \hat{W}_1 + 2\hat{W}_0 \varsigma \cos\phi \end{aligned} \tag{16}$$

And for the fourth order as:

$$\begin{aligned}
U_4 &= -\bar{U}_3 + \bar{U}_2\varsigma\cos\phi - \bar{U}_1\varsigma^2\cos^2\phi + \bar{U}_0\varsigma^3\cos^3\phi - \hat{U}_2 + 2\hat{U}_1\varsigma\cos\phi - 3\hat{U}_0\varsigma^2\cos^2\phi \\
V_4 &= -\bar{V}_3 + \bar{V}_2\varsigma\cos\phi - \bar{V}_1\varsigma^2\cos^2\phi + \bar{V}_0\varsigma^3\cos^3\phi - \hat{V}_2 + 2\hat{V}_1\varsigma\cos\phi - 3\hat{V}_0\varsigma^2\cos^2\phi \\
W_4 &= -\bar{W}_3 + \bar{W}_2\varsigma\cos\phi - \bar{W}_1\varsigma^2\cos^2\phi + \bar{W}_0\varsigma^3\cos^3\phi - \hat{W}_2 + 2\hat{W}_1\varsigma\cos\phi - 3\hat{W}_0\varsigma^2\cos^2\phi
\end{aligned} \tag{17}$$

Navier functions of order $k(k = 0, 1, 2, \ldots)$ in Eqs. (13)–(17) are defined in "Appendix 1." Combining Eqs. (4), (9) and (12), the formulas for calculating the stress components of order $k$, valid for $k = 0, 1, 2, 3$ and 4 are determined as:

$$\begin{aligned}
\tau_{\varsigma\varsigma k} &= \frac{\partial u_k}{\partial\varsigma} + \frac{\nu}{1-2\nu}\left(\psi_k + \chi_{k-1} - \varsigma\cos\phi\chi_{k-2} + \varsigma^2\cos^2\phi\chi_{k-3} - \varsigma^3\cos^3\phi\chi_{k-4}\right) \\
\tau_{\phi\phi k} &= \left(\frac{u_k}{\varsigma} + \frac{1}{\varsigma}\frac{\partial v}{\partial\phi}\right) + \frac{\nu}{1-2\nu}\left(\psi_k + \chi_{k-1} - \varsigma\cos\phi\chi_{k-2} + \varsigma^2\cos^2\phi\chi_{k-3} - \varsigma^3\cos^3\phi\chi_{k-4}\right) \\
\tau_{\theta\theta k} &= \frac{\nu}{1-2\nu}\psi_k + \frac{1-\nu}{1-2\nu}\left(\chi_{k-1} - \varsigma\cos\phi\chi_{k-2} + \varsigma^2\cos^2\phi\chi_{k-3} - \varsigma^3\cos^3\phi\chi_{k-4}\right) \\
\tau_{\varsigma\phi k} &= \frac{1}{2}\left(\frac{1}{\varsigma}\frac{\partial u_k}{\partial\phi} + \frac{\partial v_k}{\partial\varsigma} - \frac{v_k}{\varsigma}\right) \\
\tau_{\varsigma\theta k} &= \frac{1}{2}\left(\begin{array}{l}\frac{\partial w_k}{\partial\varsigma} + \left(\frac{\partial u_{k-1}}{\partial\theta} - w_{k-1}\cos\phi\right) - \varsigma\cos\phi\left(\frac{\partial u_{k-2}}{\partial\theta} - w_{k-2}\cos\phi\right) \\ +\varsigma^2\cos^2\phi\left(\frac{\partial u_{k-3}}{\partial\theta} - w_{k-3}\cos\phi\right) - \varsigma^3\cos^3\phi\left(\frac{\partial u_{k-4}}{\partial\theta} - w_{k-4}\cos\phi\right)\end{array}\right) \\
\tau_{\phi\theta k} &= \frac{1}{2}\left(\begin{array}{l}\frac{1}{\varsigma}\frac{\partial w_k}{\partial\phi} + \left(\frac{\partial v_{k-1}}{\partial\theta} + w_{k-1}\sin\phi\right) - \varsigma\cos\phi\left(\frac{\partial v_{k-2}}{\partial\theta} + w_{k-2}\sin\phi\right) \\ +\varsigma^2\cos^2\phi\left(\frac{\partial v_{k-3}}{\partial\theta} + w_{k-3}\sin\phi\right) - \varsigma^3\cos^3\phi\left(\frac{\partial v_{k-4}}{\partial\theta} + w_{k-4}\sin\phi\right)\end{array}\right)
\end{aligned} \tag{18}$$

We should mention that functions with subscripts of negative indices are considered zero in the equations presented above.

The method of successive approximation is a useful and powerful numerical method for obtaining solutions to governing equations (Eq. 7), but it is difficult to justify precisely. The series solutions are local in $\varepsilon$ and global in $r$. When $\varepsilon$ is small, one obtains a good approximation to the solution by the summation of the first few terms of the series. When $\varepsilon$ is not small, it may still be possible to obtain a good approximation to the solution with slow convergence rate. Selecting the parameter $\varepsilon$ should be done consistently; $\varepsilon$ is chosen based on geometric parameters in the problem, i.e., $R$, $a$ and $b$. Since the bending radius $R$ is constant, $R$ could be one of the parameters used to obtain $\varepsilon$. In addition, radii $a$ and $b$ are also among the choices for obtaining $\varepsilon$. First, the smaller parameter, which is $a$, is selected to check the convergence of the displacement series. If the convergence is not achieved, the other parameter, which is $b$, will be selected. In general, it is possible to introduce $\varepsilon$ in a way that the zeroth-order solution is obtained as a closed-form expression. In practice, only the first few terms of the solution series can be conveniently calculated since the iteration procedure becomes increasingly cumbersome when the order increases. It is necessary to select a suitable parameter $\varepsilon$ which leads to a fast convergence for the final solution. The solution obtained by the method of successive approximation converges only for the values of $\varepsilon$ smaller than the radius of convergence of the displacement series.

It is clear from Eqs. (13)–(17) that the zeroth-order governing equations are homogenous equations. The right-hand side terms for orders greater than zero include portions from the lower orders. There is only a complementary solution for the zeroth-order governing equations. For orders greater than zero, the solutions consist of complementary and particular parts. The complementary part is determined from the homogeneous part of the same order's governing equations. The particular part is derived in order to satisfy the right-hand side terms of the governing equations. The particular part is developed using trial displacement functions with free constants, similar to the right-hand side terms of the governing equations of the same order.

The procedure for solving a specific problem is given as follows: (a) Solutions are proposed successively for the different orders, starting from the zeroth order; (b) the zeroth-order solution is selected from the complementary solution; (c) the particular part is arranged using trial functions. The displacement functions for the same order are obtained by summing the complementary and particular parts. The constants in the complementary solution of each order are determined separately from the boundary conditions; (d) the total solution is found by adding the particular and complementary solutions of all the orders multiplied by the

corresponding power of $\varepsilon$; and (e) constants remained in the total solution are determined from boundary conditions.

## 4 General solution for different series of load case scenarios

The complementary solution for the displacement components is presented in the following form:

$$\begin{aligned} u_0 &= a\varsigma^m \cos(n\phi)\, F(\theta) \\ v_0 &= b\varsigma^m \sin(n\phi)\, F(\theta) \\ w_0 &= c\varsigma^{\bar{m}} \cos(n\phi)\, G(\theta) \end{aligned} \tag{19}$$

where the functions $F(\theta)$ and $G(\theta)$ are unknown which are obtained by boundary conditions. The quantities $a$, $b$, $c$, $m$, $\bar{m}$ and $n$ are constants determined by the zeroth-order Navier equations, Eq. (13), and stress-free boundary conditions on the free surfaces leading to:

$$\begin{aligned} u_0 &= \left[ \begin{array}{l} a_0\varsigma^{-1} + b_0\varsigma + \left\{a_1 + b_1(1-4\nu)\varsigma^2 + c_1\varsigma^{-2} + d_1(3-4\nu)\ln\varsigma\right\}\cos\phi \\ \quad + \sum_{n=2}^{\infty}\left\{a_n\varsigma^{n-1} + b_n(2-n-4\nu)\varsigma^{n+1} + c_n\varsigma^{-(n+1)} + d_n(2-n+4\nu)\varsigma^{-(n-1)}\right\}\cos n\phi \end{array} \right] F(\theta) \\ v_0 &= \left[ \begin{array}{l} \left\{-a_1 + b_1(5-4\nu)\varsigma^2 + c_1\varsigma^{-2} - d_1(3-4\nu)\ln\varsigma - d_1\right\}\sin\phi \\ \quad + \sum_{n=2}^{\infty}\left\{-a_n\varsigma^{n-1} + b_n(4+n-4\nu)\varsigma^{n+1} + c_n\varsigma^{-(n+1)} + d_n(4-n-4\nu)\varsigma^{-(n-1)}\right\}\sin n\phi \end{array} \right] F(\theta) \\ w_0 &= \left[ e_0 + f_0\ln\varsigma + \left\{e_1\varsigma^{-1} + f_1\varsigma\right\}\cos\phi + \sum_{n=2}^{\infty}\left\{e_n\varsigma^{-n} + f_n\varsigma^n\right\}\cos n\phi \right] G(\theta) \end{aligned} \tag{20}$$

where constant quantities $a_0$, $b_0$, $a_1$, $b_1$, $c_1$, $d_1$, $e_0$, $f_0$, $e_1$, $f_1$, $a_n$, $b_n$, $c_n$, $d_n$, $e_n$ and $f_n$ are obtained by applying boundary conditions [Eq. (21)]. The abovementioned detailed solution is presented here for a 90° thick isotropic curved tube subjected to axial load $F_z$, torque $T_z$ and bending moment $M_y$, in the plane of the curved tube as shown in Fig. 1. On the free curved surfaces ($\varsigma = 1$ and $\varsigma = a/b$), the following boundary conditions must be satisfied:

$$\tau_{\varsigma\varsigma k} = \tau_{\varsigma\phi k} = \tau_{\varsigma\theta k} = 0 \tag{21}$$

On the end surfaces $\theta = 0°$ and 90°

$$M_y = M_0 + \varepsilon M_1 + \varepsilon^2 M_2 + \varepsilon^3 M_3 + \ldots \tag{22a}$$

$$T_z = T_0 + \varepsilon T_1 + \varepsilon^2 T_2 + \varepsilon^3 T_3 + \ldots \tag{22b}$$

$$F_z = F_0 + \varepsilon F_1 + \varepsilon^2 F_2 + \varepsilon^3 F_3 + \ldots \tag{22c}$$

where $M_y$, $F_z$ and $T_z$ are the applied pure bending moment, axial load and torque, respectively. These boundary conditions, Eq. (21), on the free curved surfaces are applied by each order separately. In order to consider the boundary conditions given in Eq. (22), on the both end surfaces, the functions $F(\theta)$ and $G(\theta)$ are chosen as:

$$F(\theta) = \cos\theta,\ G(\theta) = \sin\theta \tag{23}$$

### 4.1 The zeroth-order solution

The zeroth-order governing equations are homogeneous equations as follows:

$$\begin{aligned} &\nabla^2 u_0 - \frac{u_0}{\varsigma^2} - \frac{2}{\varsigma^2}\frac{\partial v_0}{\partial\phi} + \frac{1}{1-2\nu}\frac{\partial\psi_0}{\partial\varsigma} = 0 \\ &\nabla^2 v_0 - \frac{v_0}{\varsigma^2} + \frac{2}{\varsigma^2}\frac{\partial u_0}{\partial\phi} + \frac{1}{1-2\nu}\frac{1}{\varsigma}\frac{\partial\psi_0}{\partial\phi} = 0 \\ &\nabla^2 w_0 = 0 \end{aligned} \tag{24}$$

Only the complementary solution is required. Considering Eq. (20), the zeroth-order displacement components are selected as:

Complementary solution

$$\begin{aligned} u_0 &= (a_1)\cos\phi\cos\theta \\ v_0 &= (-a_1)\sin\phi\cos\theta \\ w_0 &= 0 \end{aligned}$$

Particular solution

$$\begin{aligned} u_0 &= 0 \\ v_0 &= 0 \\ w_0 &= 0 \end{aligned} \tag{25}$$

Considering the boundary conditions on the free inner and outer surfaces, the displacement components are obtained as:

$$\begin{aligned} u_0 &= a_1\cos\phi\cos\theta \\ v_0 &= -a_1\sin\phi\cos\theta \\ w_0 &= 0 \end{aligned} \tag{26}$$

These displacement functions [Eq. (26)] express a rigid body rotation. Constant $a_1$ of the associated order is obtained by applying Eq. (22).

## 4.2 The first-order solution

For the first-order solution, the right-hand side terms of the governing equations are first obtained which are selected from Eqs. (14) and (45) and the zeroth-order displacement components. The governing equations of the first order are derived as:

$$\begin{aligned} U_1 &= -\bar{U}_0 \\ V_1 &= -\bar{V}_0 \\ W_1 &= -\bar{W}_0 \end{aligned} \quad \rightarrow \quad \begin{aligned} U_1 &= 0 \\ V_1 &= 0 \\ W_1 &= 0 \end{aligned} \tag{27}$$

The first-order solution contains a complementary and a particular part. The complementary part is chosen from Eq. (20). The particular part is obtained using trial functions. Considering together the complementary and particular parts, the first-order displacement components are derived:

$$\begin{aligned} u_1 &= \left(a_0\varsigma^{-1} + b_0\varsigma\right)\cos\theta \\ v_1 &= 0 \\ w_1 &= (e_0 + f_0\ln\varsigma)\sin\theta \end{aligned} \tag{28}$$

The free constants in Eq. (28) are derived by applying the stress components $\tau_{\varsigma\varsigma 1} = \tau_{\varsigma\theta 1} = \tau_{\varsigma\phi 1} = 0$ corresponding to the boundary conditions. The constants $a_0$, $b_0$, $e_0$ and $f_0$ are zero. Substituting these constants into Eq. (28), the first-order displacement components are obtained as:

$$\begin{aligned} u_1 &= 0 \\ v_1 &= 0 \\ w_1 &= 0 \end{aligned} \tag{29}$$

### *4.2.1 The second-order solution*

The second-order governing equations are determined as:

$$\begin{aligned} &\nabla^2 u_2 - \frac{u_2}{\varsigma^2} - \frac{2}{\varsigma^2}\frac{\partial v_2}{\partial\phi} + \frac{1}{1-2\nu}\frac{\partial\psi_2}{\partial\varsigma} = \frac{3-4\upsilon}{1-2\nu}a_1\cos\phi\cos\theta \\ &\nabla^2 v_2 - \frac{v_2}{\varsigma^2} + \frac{2}{\varsigma^2}\frac{\partial u_2}{\partial\phi} + \frac{1}{1-2\nu}\frac{1}{\varsigma}\frac{\partial\psi_2}{\partial\phi} = \frac{4\upsilon-3}{1-2\nu}a_1\sin\phi\cos\theta \\ &\nabla^2 w_2 = \frac{4\upsilon-3}{1-2\nu}a_1\sin\theta \end{aligned} \tag{30}$$

The second-order displacement components are selected as:

Complementary solution

$$\begin{aligned} u_2 &= \left[b_1\,(1-4\nu)\,\varsigma^2 + c_1\varsigma^{-2} + d_1\,(3-4\nu)\ln\varsigma\right]\cos\phi\cos\theta \\ v_2 &= \left[b_1\,(5-4\nu)\,\varsigma^2 + c_1\varsigma^{-2} - d_1\,(3-4\nu)\ln\varsigma - d_1\right]\sin\phi\cos\theta \\ w_2 &= \left[e_1\varsigma^{-1} + f_1\varsigma\right]\cos\phi\sin\theta \end{aligned}$$

Particular solution

$$\begin{aligned} u_2 &= -a_1\varsigma^2\cos\phi\cos\theta \\ v_2 &= a_1\varsigma^2\sin\phi\cos\theta \\ w_2 &= 0 \end{aligned} \tag{31}$$

Subsequently, the stress components are presented as:

$$\begin{aligned} \tau_{\varsigma\varsigma 2} &= \left[2b_1\varsigma - 2c_1\varsigma^{-3} + (3-2\nu)\,d_1\varsigma^{-1} + \frac{2-\upsilon}{1-2\upsilon}a_1\varsigma\right]\cos\phi\cos\theta \\ \tau_{\varsigma\phi 2} &= \left[2b_1\varsigma - 2c_1\varsigma^{-3} - (1-2\nu)\,d_1\varsigma^{-1} + a_1\varsigma\right]\sin\phi\cos\theta \\ \tau_{\varsigma\theta 2} &= \frac{1}{2}\left[-e_1\varsigma^{-2} + f_1\right]\cos\phi\sin\theta - \frac{1}{2}a_1\varsigma\cos^2\phi\sin\theta \end{aligned} \tag{32}$$

where $b_1$, $c_1$, $d_1$, $e_1$ and $f_1$ are free constants. By applying the appropriate boundary conditions [Eqs. (21)], the constants are obtained as:

$$c_1 = d_1 = e_1 = f_1 = 0 \quad \text{and} \quad b_1 = -\frac{1}{2}\frac{2-\upsilon}{1-2\upsilon}a_1 \tag{33}$$

Finally, the second-order displacement components are found as:

$$\begin{aligned} u_2 &= A_1\varsigma^2\cos\phi\cos\theta \\ v_2 &= B_1\varsigma^2\sin\phi\cos\theta \\ w_2 &= 0 \end{aligned} \tag{34}$$

where

$$A_1 = \frac{4\upsilon^2 - 13\upsilon + 4}{4\upsilon - 2}a_1, \quad B_1 = \frac{4\upsilon^2 - 9\upsilon + 8}{4\upsilon - 2}a_1 \tag{35}$$

*4.2.2 The third-order solution*

The third-order governing equations are derived from Eqs. (16) and (45). On the right-hand sides of the first two of these equations, there are two sets of terms. The governing equations of the third-order are developed as:

$$\begin{aligned} &\nabla^2 u_3 - \frac{u_3}{\varsigma^2} - \frac{2}{\varsigma^2}\frac{\partial v_3}{\partial\phi} + \frac{1}{1-2\nu}\frac{\partial\psi_3}{\partial\varsigma} = \frac{1}{2}\left[A_{11} - B_{11}\right]\varsigma\cos 2\phi\cos\theta \\ &\nabla^2 v_3 - \frac{v_3}{\varsigma^2} + \frac{2}{\varsigma^2}\frac{\partial u_3}{\partial\phi} + \frac{1}{1-2\nu}\frac{1}{\varsigma}\frac{\partial\psi_3}{\partial\phi} = C_{11}\varsigma\sin 2\phi\cos\theta \\ &\nabla^2 w_3 = D_{11}\varsigma\cos\phi\sin\theta \end{aligned} \tag{36}$$

As a result, the particular solution for Eq. (36) is obtained as:

$$\begin{aligned} u_{3p} &= A_{22}\varsigma^3\cos 2\phi\cos\theta \\ v_{3p} &= C_{22}\varsigma^3\sin 2\phi\cos\theta \\ w_{3p} &= D_{22}\varsigma^3\cos\phi\sin\theta \end{aligned} \tag{37}$$

The coefficients appearing in Eqs. (36) and (37) are defined in "Appendix 2." Therefore, the third-order solution is presented in the following form:

$$\begin{aligned} u_3 &= \left[a_2\varsigma + b_2\left(1-4\nu\right)\varsigma^3 + c_2\varsigma^{-3} + d_2\left(3-4\nu\right)\varsigma^{-1} + A_{22}\varsigma^3\right]\cos 2\phi\cos\theta \\ v_3 &= \left[-a_2\varsigma + b_2\left(6-4\nu\right)\varsigma^3 + c_2\varsigma^{-3} + d_2\left(2-4\nu\right)\varsigma^{-1} + C_{22}\varsigma^3\right]\sin 2\phi\cos\theta \\ w_3 &= \left[e_2\varsigma^{-2} + f_2\varsigma^2 + D_{22}\varsigma^3\right]\cos\phi\sin\theta \end{aligned} \tag{38}$$

and

$$\begin{aligned} \tau_{\varsigma\varsigma 3} &= \left[a_2 - 3c_2\varsigma^{-4} + 4d_2\varsigma^{-2}\right]\cos 2\phi\cos\theta + \left[3A_{22} + \frac{\upsilon}{1-2\upsilon}\left(4A_{22} + 2C_{22} + \frac{1}{2}a_1\right)\right]\varsigma^2\cos 2\phi\cos\theta \\ \tau_{\varsigma\phi 3} &= \left[-a_2 + 6b_2\varsigma^2 - 3c_2\varsigma^{-4} + 2d_2\varsigma^{-2}\right]\sin 2\phi\cos\theta + \left(C_{22} - A_{22}\right)\varsigma^2\sin 2\phi\cos\theta \\ \tau_{\varsigma\theta 3} &= \frac{1}{2}\left[-2e_2\varsigma^{-3} + 2f_2\varsigma\right]\cos\phi\sin\theta + \frac{1}{2}\left[\left(\frac{4\upsilon^2 - 13\upsilon + 4}{2-4\upsilon}\right)a_1 + 3D_{22}\right]\varsigma^2\cos\phi\sin\theta \end{aligned} \tag{39}$$

where $a_2$, $b_2$, $c_2$, $d_2$, $e_2$ and $f_2$ are constants presented in "Appendix 3" which are obtained applying the boundary conditions, Eq. (21), and governing equations, Eq. (36). These constants are obtained in terms of the material property, Poisson ratio ($\upsilon$) and the aspect ratio ($a/b$).

### *4.2.3 The fourth-order solution*

The fourth-order governing equations are derived from Eqs. (17) and (45). The governing equations for the fourth-order are expressed as:

$$\begin{aligned} \nabla^2 u_4 - \frac{u_4}{\varsigma^2} - \frac{2}{\varsigma^2}\frac{\partial v_4}{\partial\phi} + \frac{1}{1-2\nu}\frac{\partial\psi_4}{\partial\varsigma} &= \left[L_1\varsigma^2 + L_2\varsigma^{-4} + L_3\varsigma^{-2}\right]\cos 3\phi\cos\theta \\ &\quad + \left[L_4 + L_5\varsigma^2 + L_6\varsigma^{-2}\right]\cos\phi\cos\theta \\ \nabla^2 v_4 - \frac{v_4}{\varsigma^2} + \frac{2}{\varsigma^2}\frac{\partial u_4}{\partial\phi} + \frac{1}{1-2\nu}\frac{1}{\varsigma}\frac{\partial\psi_4}{\partial\phi} &= \left[L_7\varsigma^2 + L_8\varsigma^{-4} + L_9\varsigma^{-2}\right]\sin 3\phi\cos\theta \\ &\quad + \left[L_{10} + L_{11}\varsigma^2 + L_{12}\varsigma^{-2} + L_{13}\varsigma^{-3} + L_{14}\varsigma\right]\sin\phi\cos\theta \\ \nabla^2 w_4 &= \left[L_{17}\varsigma^2 + L_{18}\varsigma^{-2} + L_{15}\varsigma^{-3} + L_{16}\varsigma\right]\cos 2\phi\sin\theta + \left[L_{19} + L_{20}\right]\sin\theta \end{aligned} \tag{40}$$

where the coefficients appearing in Eq. (40) are defined in "Appendix 4." For the complementary parts of $u_4$ and $v_4$, the third harmonic solution is selected, while for $w_4$ the second harmonic solution is chosen. Subsequently, the fourth-order solution is expressed as:

$$\begin{aligned} u_4 &= \left[a_3\varsigma^2 - b_3\left(1+4\nu\right)\varsigma^4 + c_3\varsigma^{-4} - d_3\left(5-4\nu\right)\varsigma^{-2}\right]\cos 3\phi\cos\theta \\ &\quad + \frac{1-2\upsilon}{20\upsilon-11}\left[L_1\varsigma^4 + L_2\varsigma^{-2} + L_3\right]\cos 3\phi\cos\theta + \frac{1-2\upsilon}{4\upsilon-3}\left[L_4\varsigma^2 + L_5\varsigma^4 + L_6\right]\cos\phi\cos\theta \\ v_4 &= \left[-a_3\varsigma^2 + b_3\left(7-4\nu\right)\varsigma^4 + c_3\varsigma^{-4} + d_3\left(1-4\nu\right)\varsigma^{-2}\right]\sin 3\phi\cos\theta \\ &\quad + \frac{1-2\upsilon}{20\upsilon-19}\left[L_7\varsigma^4 + L_8\varsigma^{-2} + L_9\right]\sin 3\phi\cos\theta + \frac{1-2\upsilon}{4\upsilon-3}\left[L_{10}\varsigma^2 + L_{11}\varsigma^4 + L_{12} + L_{13}\varsigma^{-1} + L_{14}\varsigma^{13}\right]\sin\phi\cos\theta \\ w_4 &= \left[e_3\varsigma^{-3} + f_3\varsigma^3\right]\cos 2\phi\sin\theta - \frac{1}{4}\left[L_{15}\varsigma^{-1} + L_{16}\varsigma^3 + L_{18} + L_{17}\varsigma^4\right]\cos 2\phi\sin\theta \end{aligned} \tag{41}$$

and

$$\begin{aligned} \tau_{\varsigma\varsigma 4} &= \left[2a_3\varsigma - 4b_3\varsigma^3 - 4c_3\varsigma^{-5} + 10d_3\varsigma^{-3}\right]\cos 3\phi\cos\theta + H_1\left(\varsigma\right)\cos 3\phi\cos\theta \\ \tau_{\varsigma\phi 4} &= \left[-2a_3\varsigma + 12b_3\varsigma^3 - 4c_3\varsigma^{-5} + 6d_3\varsigma^{-3}\right]\sin 3\phi\cos\theta + H_2\left(\varsigma\right)\sin 3\phi\cos\theta \\ \tau_{\varsigma\theta 4} &= \left[-\frac{3}{2}e_3\varsigma^{-4} + \frac{3}{2}f_3\varsigma^2\right]\cos 2\phi\sin\theta + H_3\left(\varsigma\right)\cos 2\phi\sin\theta \end{aligned} \tag{42}$$

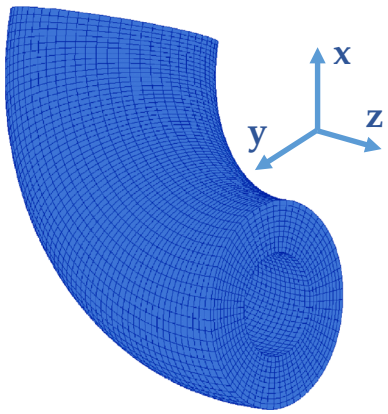


**Fig. 3** Modeling of thick isotropic curved tubes using ANSYS

where the coefficients appearing in Eq. (42) are defined in "Appendix 4." It should be noted that $a_3$, $b_3$, $c_3$, $d_3$, $e_3$ and $f_3$ are free constants presented in "Appendix 5." These constants are obtained by applying the boundary conditions presented in Eq. (21) and governing equations given Eq. (40). Integrating the stress components of $\tau_{\theta\theta}$ and $\tau_{\theta\phi}$ up to the fourth-order over the both end surfaces leads to:

$$M_y = M_0 + \varepsilon M_1 + \varepsilon^2 M_2 + \varepsilon^3 M_3 + \varepsilon^4 M_4$$

$$M_k = \int_{a/c}^{b/c} \int_0^{2\pi} (\tau_{\theta\theta k} \varsigma \cos\phi)\, \varsigma d\phi d\varsigma \quad \text{at} \quad \theta = 0^\circ, 90^\circ \tag{43a}$$

$$T_z = T_0 + \varepsilon T_1 + \varepsilon^2 T_2 + \varepsilon^3 T_3 + \varepsilon^4 T_4$$

$$T_k = \int_{a/c}^{b/c} \int_0^{2\pi} \left(\tau_{\theta\phi k} \varsigma\right) \varsigma d\phi d\varsigma \quad \text{at} \quad \theta = 0^\circ, 90^\circ \tag{43b}$$

$$F_z = F_0 + \varepsilon F_1 + \varepsilon^2 F_2 + \varepsilon^3 F_3 + \varepsilon^4 F_4$$

$$F_k = \int_{a/c}^{b/c} \int_0^{2\pi} (\tau_{\theta\theta k})\, \varsigma d\phi d\varsigma \quad \text{at} \quad \theta = 0^\circ, 90^\circ \tag{43c}$$

The total solution for thick isotropic curved tubes subjected to combined mechanical loads is developed by considering the solutions of all the orders and substituting them into Eqs. (9) and (10).

## 5 FEM analysis

The thick isotropic curved tubes are modeled by ANSYS finite element software using SOLID185 element (See Fig. 3). The SOLID185 element, which is a three-dimensional element consisting eight nodes with three degrees of freedom at each node, is used for the finite element simulation. Using the finite element analysis, stress distributions within the tube are calculate to compare with those results obtained by the proposed theoretical method mentioned in Sects. 2, 3 and 4. The mesh sensitivity study is conducted; mesh refining is performed two times while the element aspect ratio is kept constant. It is noted that for the initial analysis, 36000 elements (60 axial × 60 circumferential × 10 thickness directions) are used to model the structure. During the first mesh refinement, meshes through the thickness and circumferential directions are refined twice as much as the initial mesh (144,000 elements). For the second refinement, the axial and circumferential directions are refined twice as much as the initial mesh and the thickness direction is refined four times as much as the initial mesh to model the curved tube by 576,000 elements.

## 6 Results and discussion

In this section, numerical results are presented and discussed for thick isotropic curved tubes under axial load, torque and bending moment (see Fig. 1) with the following geometric and material parameters (unless otherwise mentioned):

$$\theta = 90^\circ, \quad b/a = 2, \quad R/a = 5, \quad \upsilon = 0.3, \quad c = a \quad \text{and} \quad E = 206\,\text{GPa} \tag{44}$$

We should note that the thick isotropic curved tube investigated here is subjected to all loads simultaneously. In addition, the radius of convergence of a series is defined as the limit value of $u_{k+1}/u_k$ when $k$ tends to infinity. The value of the radius of convergence of three series of displacement components [i.e., $u$, $v$ and $w$ in Eq. (9)] is larger than one. The small parameter $\varepsilon$ is selected as the ratio of outside radius of the cross section to the mean toroidal radius $(a/R)$ which is smaller than the radius of convergence and as a result, the numerical successive approximation technique converges.

### 6.1 Comparison of the present method with FEM

The convergence study is performed to determine how many orders of successive approximation are required to obtain accurate results. Table 1 presents the radial and hoop stresses obtained by the proposed method with different orders and the finite element analysis. It is worth mentioning that the stresses in Table 1 are normalized according to Eq. (2) and obtained at $\phi = 180^\circ$, $\theta = 0^\circ$ and $\varsigma = 0.25$ of the isotropic curved tube. It is seen that by increasing the number of orders in the successive approximation method, the difference between the obtained results and FEM predictions decreases. Since the differences for the third and fourth orders in are close, the solutions up to the third-order are chosen in this paper for the presentation of results in the rest of the paper.

The radial ($\tau_{\varsigma\varsigma}$) and hoop ($\tau_{\phi\phi}$) stresses on the middle surface ($\varsigma = 0.5$) of the isotropic curved tube obtained by the present method and FEM (*ANSYS*) are compared in Fig. 4. Close agreement between the proposed semi-analytical methodology and FEM results is obtained. It is worthwhile noting that analyzing the thick isotropic curved tube with the initial mesh takes 880 s while it takes 1100 and 2000 s when the first and second refinement are used, respectively. The analysis using the proposed semi-analytical methodology, however, is much faster and it takes only 120 s.

**Table 1** Convergence study for the isotropic curved tube

| Normalized stress | Order of successive approx | | | | |
|---|---|---|---|---|---|
| | Up to the first-order (difference %) | Up to the second-order (difference %) | Up to the third-order (difference %) | Up to the fourth-order (difference %) | FEM |
| Radial stress | 0.37 (25%) | 0.44 (12%) | 0.48 (4%) | 0.49 (3%) | 0.5 |
| Hoop stress | 1.63 (27%) | 1.94 (13%) | 2.10 (6%) | 2.12 (5%) | 2.23 |

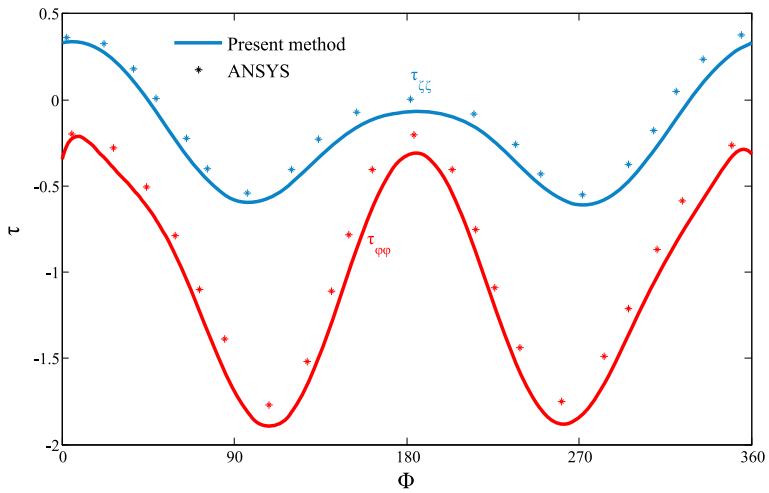


**Fig. 4** Comparison of the radial stresses ($\tau_{\varsigma\varsigma}$) and hoop stresses ($\tau_{\phi\phi}$) on the middle surface ($\varsigma = 0.5$) of the isotropic curved tube obtained by the present method and FEM (ANSYS)

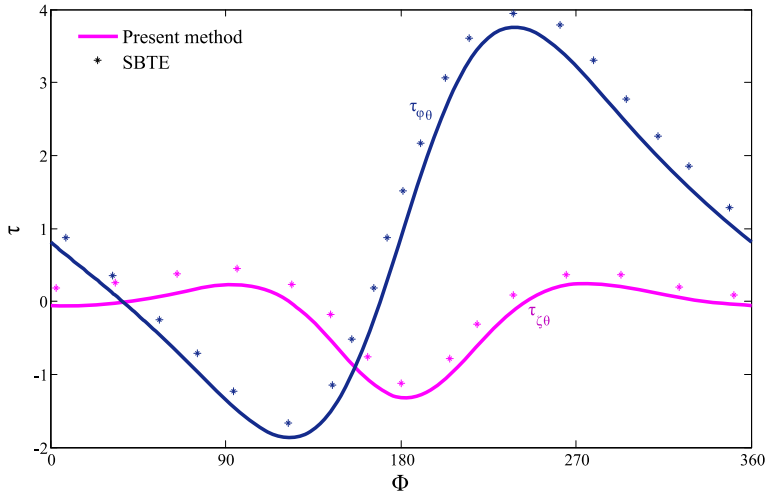


**Fig. 5** Comparison of the shear stresses ($\tau_{\phi\theta}$) and hoop stresses ($\tau_{\varsigma\theta}$) on the middle surface ($\varsigma = 0.5$) of the isotropic curved tube obtained by the present method and SBTE

### 6.2 Comparison of the present method with SBTE

The shear stresses of $\tau_{\phi\theta}$ and $\tau_{\varsigma\theta}$ on the middle surface ($\varsigma = 0.5$) of the isotropic curved tube obtained by both the proposed methodology and SBTE are shown in Fig. 5. Close agreement between the semi-analytical analysis and SBTE results is observed. It is seen that the numerical results obtained by SBTE and FEM are about 5% higher than those predicted by the proposed method (see Figs. 4, 5).

### 6.3 Advantages of the proposed methodology

The most important advantage of the present methodology is that required inputs for the modeling and analyzing of thick isotropic curved structures are simple, while the methodology is easy to use and fast to run. Using the present method, one just needs to simply define the dimensions the beginning of the program. It is obvious that the modeling of curved structures using FEM takes much longer compared to the present methodology. One of the advantages of the proposed methodology is the accuracy of the obtained numerical results. While using FEM for the parametric study of curved tubes is cumbersome, the proposed methodology can be applied easily for parametric studies with a low computational cost. For example, to study the effect of thickness on the stress and strain distributions using FEM, it is necessary to model the geometry for different thicknesses and obviously it takes much longer for FEM than using the present methodology.

The present methodology has the advantages of obtaining directly the displacements as well as the stresses as compared with SBTE. The zeroth-order displacement functions required for starting the method of successive approximation are formulated based on the general mechanical knowledge. We should remark that the displacement components are important information for considering special constraints and for fracture analysis. We should note that the present methodology could be extended to study thick curved tubes with anisotropic mechanical properties. In order to model a composite curved tube, it is needed to use the constitutive equations for orthotropic materials, and a similar approach can be developed for stress analysis [30–32].

### 6.4 Stress distributions

Performed discussion here is on thick isotropic curved tubes subjected to axial load, torque and bending moment. The stress distributions are discussed through several numerical examples based on the present method.

The distributions of the normalized radial ($\tau_{\varsigma\varsigma}$) and shear ($\tau_{\varsigma\theta}$) stresses over cross section on the middle surface ($\varsigma = 0.5$) of the thick isotropic curved tube are presented in Fig. 6. The numerical results for the radial stress ($\tau_{\varsigma\varsigma}$) show the symmetric behavior while the shear stress distributions are not symmetric. It is

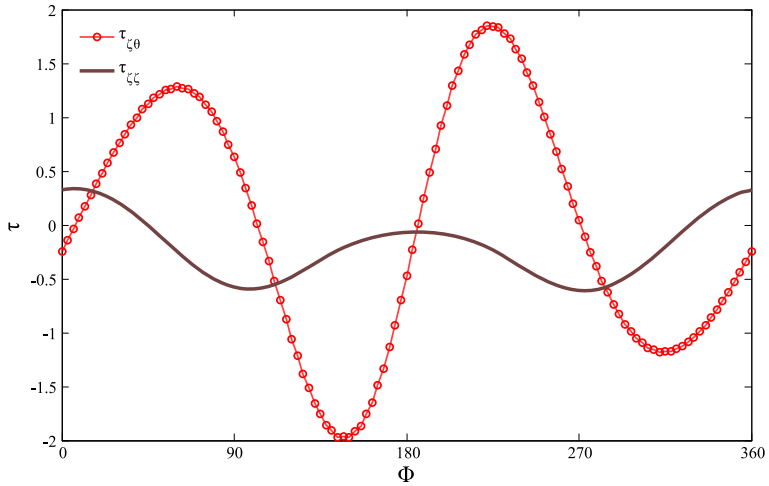


**Fig. 6** Distributions of the normalized radial stresses ($\tau_{\varsigma\varsigma}$) and shear stresses ($\tau_{\varsigma\theta}$) over cross section on the middle surface ($\varsigma = 0.5$) of the isotropic curved tube

seen that the maximum magnitudes of the radial stress ($\tau_{\varsigma\varsigma}$) occur at $\phi = 90°$ and 270° while the maximum magnitudes of the shear stress ($\tau_{\varsigma\theta}$) occur at $\phi = 150°$. It is found that the maximum magnitudes of the shear stress ($\tau_{\varsigma\theta}$) are greater than those of the radial stress ($\tau_{\varsigma\varsigma}$).

Figures 7, 8 and 9 show the distributions of the normalized hoop ($\tau_{\phi\phi}$), longitudinal ($\tau_{\theta\theta}$) and shear ($\tau_{\phi\theta}$) stresses over the tube cross section in the inside ($\varsigma = a/b$), middle ($\varsigma = 0.5$) and outside ($\varsigma = 1$) surfaces of the isotropic curved tube, respectively. As depicted in Figs. 7, 8 and 9, the maximum values of the hoop stress ($\tau_{\phi\phi}$) and the shear stress ($\tau_{\phi\theta}$) occur on the inside surface while the maximum value of the longitudinal stress ($\tau_{\theta\theta}$) occurs on the outside surface. Figure 7 shows that the hoop stress is entirely compressive on the middle surface, while the sign of hoop stress changes on the inside and outside surfaces. The maximum hoop stress on the inside and outside surfaces is compressive, and it occurs at $\phi = 180°$ on the outside surface, while it occurs at $\phi = 90°$ and 270° on the inside surface. Figure 8 shows that the maximum longitudinal stress ($\tau_{\theta\theta}$) on the outside surface is compressive, and it occurs at $\phi = 180°$, while on the middle and inside surfaces, they occur at $\phi = 0°$ and they are tensile. It is seen that the longitudinal stress is compressive at the 150° to 210° region of the curved tube cross section. In addition, the symmetric behavior is seen in Fig. 8. However, the shear stress ($\tau_{\phi\theta}$) has an anti-symmetric behavior as shown in Fig. 9. It is observed from Fig. 9 that the minimum and maximum values of all surfaces occur at the same locations which are around $\phi = 135°$ and $\phi = 225°$, respectively. In spite of the hoop stress, the behavior of the shear stress on middle surface is the same as those on the inside and outside surfaces.

Figure 10 presents the distributions of the normalized radial stress ($\tau_{\varsigma\varsigma}$) and the shear stresses of $\tau_{\varsigma\theta}$ and $\tau_{\varsigma\phi}$ along the tube thickness at $\phi = 0°$ of the thick isotropic curved tube. As it seen from Fig. 10, the radial stress ($\tau_{\varsigma\varsigma}$) and shear stresses ($\tau_{\varsigma\theta}$ and $\tau_{\varsigma\phi}$) are zero on free curved surfaces $\varsigma = 1$ and $\varsigma = a/b$ [see Eq. (21)]. The radial stress ($\tau_{\varsigma\varsigma}$) is entirely positive along the radial direction at $\phi = 0°$ while the shear stresses ($\tau_{\varsigma\phi}$ and $\tau_{\varsigma\theta}$) are negative. Observing Fig. 10, at the first, the magnitude of the radial stress ($\tau_{\varsigma\varsigma}$) along the radial direction increases from zero and then decreases toward zero. In addition, the maximum magnitudes for these stresses are placed at the different points along the tube thickness.

The distributions of the normalized longitudinal ($\tau_{\theta\theta}$), hoop ($\tau_{\phi\phi}$) and shear stresses ($\tau_{\phi\theta}$) along the tube thickness at $\phi = 0°$ of the isotropic curved tube is seen in Fig. 11. As it expected the longitudinal ($\tau_{\theta\theta}$) and the shear stresses ($\tau_{\phi\theta}$) are positive while the hoop stress ($\tau_{\phi\phi}$) starts from being positive on the inside surface to negative on the outside surface. Note that the shear stress ($\tau_{\phi\theta}$) increases along the tube thickness while the hoop stress ($\tau_{\phi\phi}$) decreases along the tube thickness. Therefore, the maximum value of the shear stress ($\tau_{\phi\theta}$) occurs on the outside surface while the maximum value of the hoop stress ($\tau_{\phi\phi}$) occurs on the inside surface. The rates are different for these stresses, and the decrease rate of the hoop stress is more than those of the others. In addition, the maximum value of the longitudinal stress ($\tau_{\theta\theta}$) occurs before the middle surface as seen in Fig. 11.

Figure 12 shows the distributions of the normalized longitudinal ($\tau_{\theta\theta}$), hoop ($\tau_{\phi\phi}$) and radial stresses ($\tau_{\varsigma\varsigma}$) along the longitudinal direction at $\phi = 0°$ and $\varsigma$=0.5 of the isotropic curved tube. It is seen that all stresses

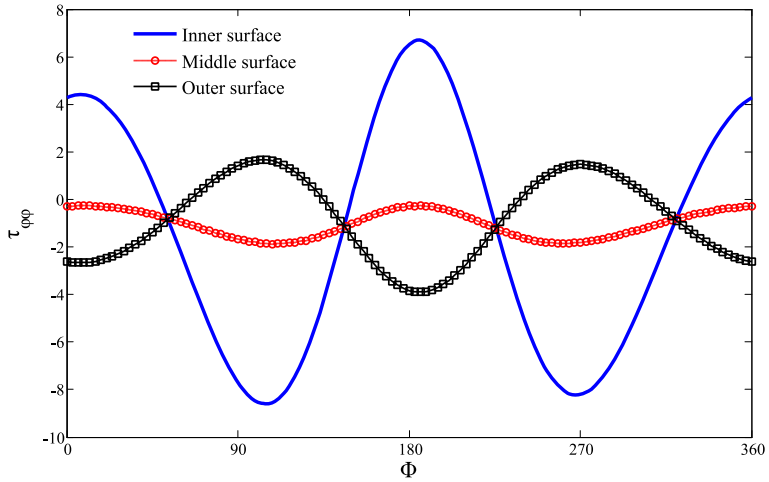


**Fig. 7** Distributions of the normalized hoop stresses ($\tau_{\phi\phi}$) over cross section on the inside ($\varsigma = a/b$), middle ($\varsigma = 0.5$) and outside surfaces ($\varsigma = 1$) of the isotropic curved tube

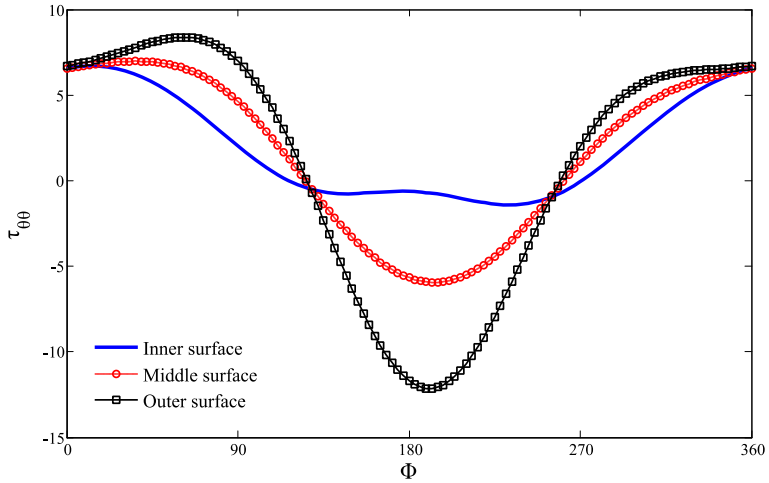


**Fig. 8** Distributions of the normalized longitudinal stresses ($\tau_{\theta\theta}$) over cross section on the inside ($\varsigma = a/b$), middle ($\varsigma = 0.5$) and outside surfaces ($\varsigma = 1$) of the isotropic curved tube

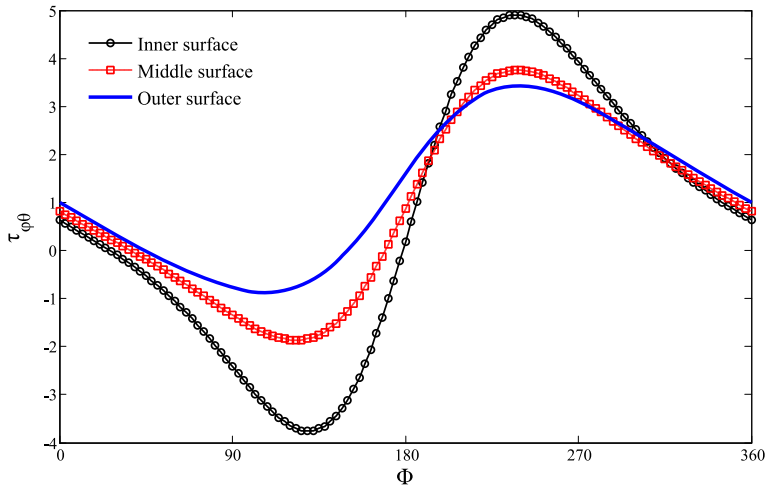


**Fig. 9** Distributions of the normalized shear stresses ($\tau_{\phi\theta}$) over cross section on the inside ($\varsigma = a/b$), middle ($\varsigma = 0.5$) and outside surfaces ($\varsigma = 1$) of the isotropic curved tube.

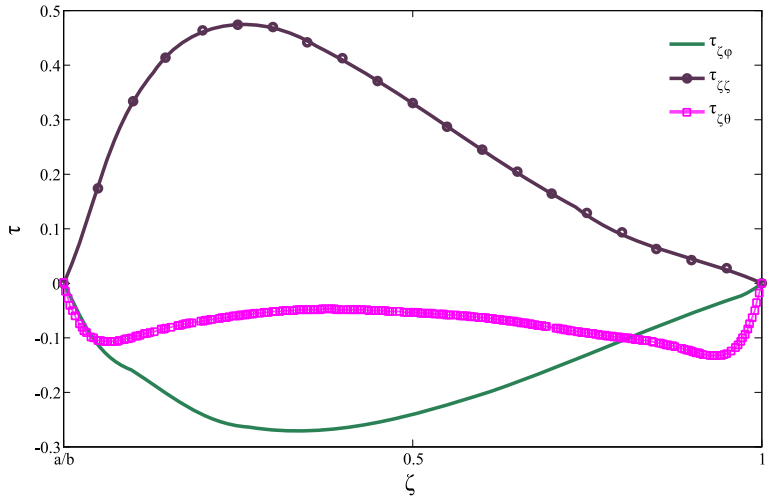


**Fig. 10** Variations of the normalized radial stress ($\tau_{\varsigma\varsigma}$) and shear stresses of $\tau_{\varsigma\theta}$, $\tau_{\varsigma\phi}$ along the radial direction at $\phi = 0°$ of the isotropic curved tube

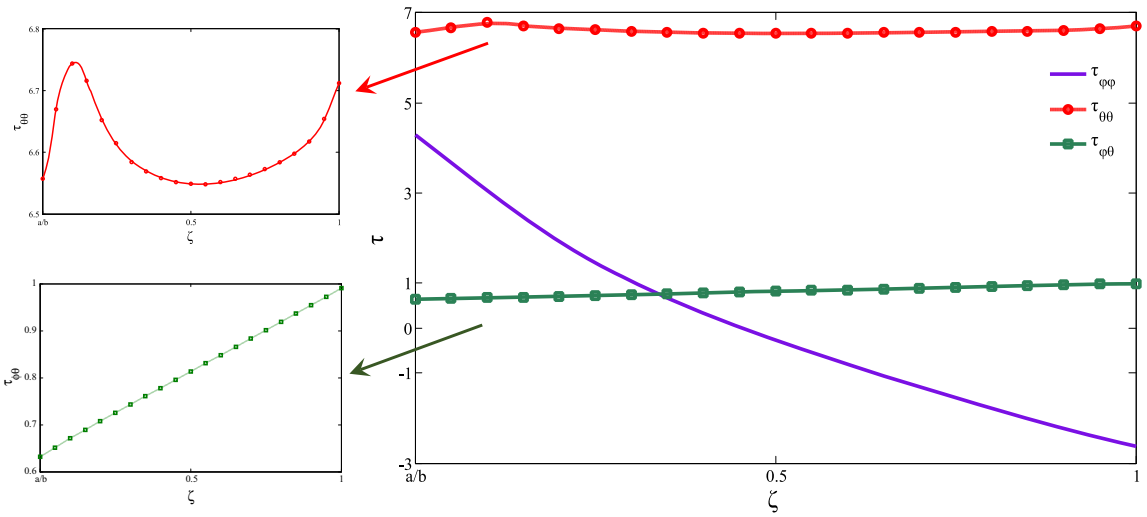


**Fig. 11** Variations of the normalized longitudinal stress ($\tau_{\theta\theta}$), hoop stress ($\tau_{\phi\phi}$) and shear stress ($\tau_{\phi\theta}$) along the radial direction at $\phi = 0°$ of the isotropic curved tube

have the symmetric behavior. The longitudinal stress ($\tau_{\theta\theta}$) decreases as it is getting closer to the middle of the curved tube while the hoop stress ($\tau_{\phi\phi}$) increases. The longitudinal and radial stresses are maximum at both sides of the curved tube (i.e., at $\theta = 0°$ and 90°) while the hoop stress ($\tau_{\phi\phi}$) is maximum at the mid-length of the curved tube (i.e., at $\theta = 45°$).

The distributions of the normalized shear stresses of $\tau_{\varsigma\theta}$, $\tau_{\varsigma\phi}$ and $\tau_{\phi\theta}$ along the longitudinal direction at $\phi = 0°$ and $\varsigma$=0.5 of the thick isotropic curved tube are presented in Fig. 13. All shear stresses have the symmetric behavior. In addition, the shear stress ($\tau_{\phi\theta}$) decreases as it is getting closer to the middle of the curved tube while the shear stress ($\tau_{\varsigma\theta}$) increases. Note that the shear stresses ($\tau_{\phi\theta}$ and $\tau_{\varsigma\phi}$) are maximum at both sides of the curved tube (i.e., at $\theta = 0°$ and 90°) while the shear stress ($\tau_{\varsigma\theta}$) is maximum at the mid-length of the curved tube (i.e., at $\theta = 45°$).

## 7 Conclusion

Toroidal elasticity is a developing three-dimensional theory which can be applied for stress analysis of thick curved tubes. A displacement-based toroidal elasticity has been used here for the stress analysis of thick

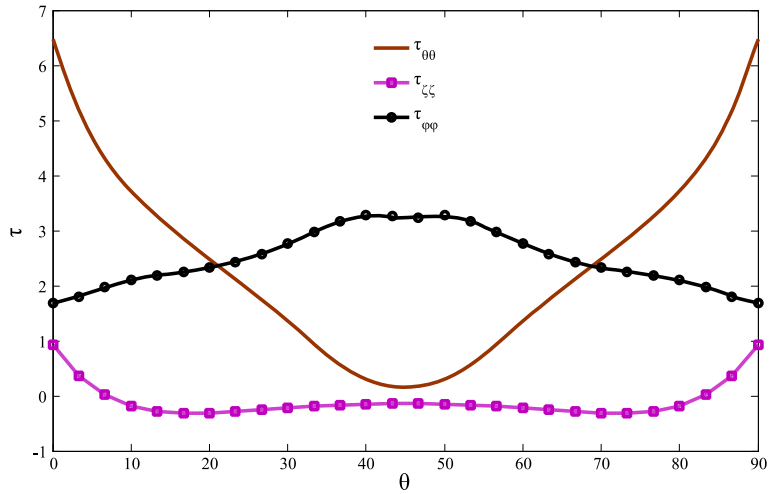


**Fig. 12** Variations of the normalized longitudinal stress ($\tau_{\theta\theta}$), hoop stress ($\tau_{\phi\phi}$) and radial stress ($\tau_{\varsigma\varsigma}$) along the longitudinal direction at $\phi = 0^\circ$ and $\varsigma = 0.5$ of the isotropic curved tube

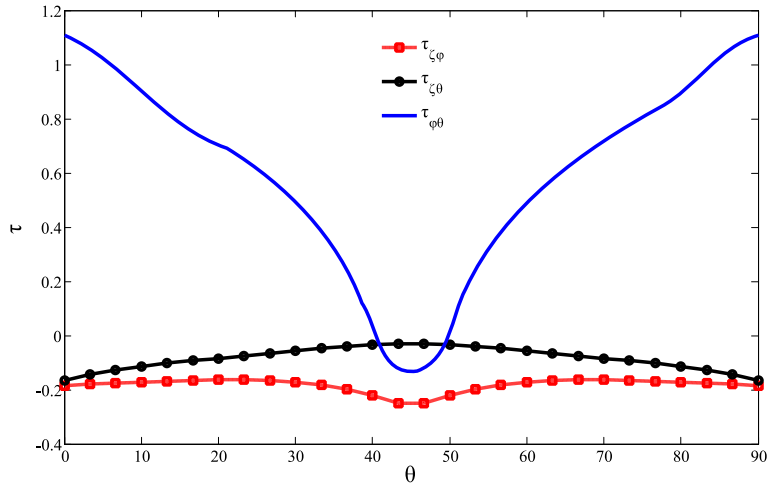


**Fig. 13** Variations of the normalized shear stresses of $\tau_{\varsigma\theta}$, $\tau_{\varsigma\phi}$ and $\tau_{\phi\theta}$ along the longitudinal direction at $\phi = 0^\circ$ and $\varsigma = 0.5$ of the isotropic curved tube

isotropic curved tubes under axial load, torque and bending moment. The successive approximation method has been employed to simplify governing equations and to reconstruct them into different orders. Moreover, the accuracy of stresses was examined comparing the present method and FEM for isotropic curved tubes. The numerical results showed good agreement between the present method with FEM and SBTE. Furthermore, the proposed method was found to be more cost-effective and accurate; therefore, it was employed to obtain stresses instead of using FEM. Finally, the conclusions obtained from the discussion are listed as following:

- The radial stress distributions show the symmetric behavior, while the shear stress distributions are not symmetric along circumferential direction.
- The maximum magnitudes of the radial stress occur at $\phi = 90^\circ$ and $270^\circ$, while the maximum magnitudes of the shear stress ($\tau_{\varsigma\theta}$) occur at $\phi = 150^\circ$. And the maximum magnitudes of the shear stress are greater than those of the radial stress.
- The maximum values of the hoop stress and the shear stress ($\tau_{\phi\theta}$) occur on the inside surface, while the maximum value of the longitudinal stress occurs on the outside surface.
- The longitudinal and radial stresses are maximum at both sides of the curved tube, while the hoop stress ($\tau_{\phi\phi}$) is maximum at the mid-length of the curved tube.

## 8 Appendices

### 8.1 Appendix 1

The coefficients appearing in Eqs. (7) and Navier functions of order $k(k = 0, 1, 2, \ldots)$ in Eqs. (13)–(17) are obtained as follows:

$$
\begin{aligned}
U_k &= \nabla^2 u_k - \frac{u_k}{\varsigma^2} - \frac{2}{\varsigma^2}\frac{\partial v_k}{\partial \phi} + \frac{1}{1-2\upsilon}\frac{\partial \psi_k}{\partial \varsigma},\\
\bar{U}_k &= \cos\phi\frac{\partial u_k}{\partial \varsigma} - \sin\phi\left(\frac{1}{\varsigma}\frac{\partial u_k}{\partial \phi} - \frac{v_k}{\varsigma}\right) + \frac{1}{1-2\upsilon}\frac{\partial \chi_k}{\partial \varsigma}\\
\hat{U}_k &= \frac{\partial^2 u_k}{\partial \theta^2} - \cos\phi\frac{\partial w_k}{\partial \theta} - \frac{2(1-\upsilon)}{1-2\upsilon}\cos\phi\chi_k\\
V_k &= \nabla^2 v_k - \frac{v_k}{\varsigma^2} + \frac{2}{\varsigma^2}\frac{\partial u_k}{\partial \phi} + \frac{1}{1-2\upsilon}\frac{1}{\varsigma}\frac{\partial \psi_k}{\partial \phi},\\
\bar{V}_k &= \cos\phi\frac{\partial v_k}{\partial \varsigma} - \sin\phi\left(\frac{1}{\varsigma}\frac{\partial v_k}{\partial \phi} + \frac{u_k}{\varsigma}\right) + \frac{1}{1-2\upsilon}\frac{1}{\varsigma}\frac{\partial \chi_k}{\partial \phi}\\
\hat{V}_k &= \frac{\partial^2 v_k}{\partial \theta^2} + \sin\phi\frac{\partial w_k}{\partial \theta} + \frac{2(1-\upsilon)}{1-2\upsilon}\sin\phi\chi_k\\
W_k &= \nabla^2 w_k, \quad \bar{W}_k = \cos\phi\frac{\partial w_k}{\partial \varsigma} - \sin\phi\frac{1}{\varsigma}\frac{\partial w_k}{\partial \phi} + \frac{1}{1-2\upsilon}\frac{\partial \psi_k}{\partial \theta}\\
\hat{W}_k &= -\frac{\partial^2 w_k}{\partial \theta^2} - w_k + \frac{3-4\nu}{1-2\upsilon}\frac{\partial \chi_k}{\partial \theta}\\
\psi_k &= \frac{\partial u_k}{\partial \varsigma} + \frac{u_k}{\varsigma} + \frac{1}{\varsigma}\frac{\partial v_k}{\partial \phi}, \quad \chi_k = u_k\cos\phi - v_k\sin\phi + \frac{\partial w_k}{\partial \theta}\\
\nabla^2(\ldots) &= \frac{\partial^2(\ldots)}{\partial \varsigma^2} + \frac{1}{\varsigma}\frac{\partial(\ldots)}{\partial \varsigma} + \frac{1}{\varsigma^2}\frac{\partial^2(\ldots)}{\partial \phi^2}
\end{aligned}
\tag{45}
$$

### 8.2 Appendix 2

The coefficients appearing in Eqs. (36) and (37) are obtained as follows:

$$
\begin{aligned}
A_{11} &= \frac{-1}{1-2\upsilon}\left[A_1(3-2\upsilon) + a_1(6-8\upsilon)\right], \quad D_{11} = \frac{1}{1-2\upsilon}\left[(3A_1 + B_1) - a_1(6-8\upsilon)\right]\\
B_{11} &= \frac{2\upsilon-3}{1-2\upsilon}B_1, \quad C_{11} = \frac{1}{1-2\upsilon}\left[\frac{1}{2}A_1(3-2\upsilon) + \frac{1}{2}A_1(1+2\upsilon) + \frac{1}{2}a_1(6-8\upsilon)\right]
\end{aligned}
\tag{46}
$$

$$
\begin{aligned}
A_{22} &= \frac{1}{2}\frac{1-2\upsilon}{6-10\upsilon}\left[B_{11} - A_{11}\right] - \frac{1}{2}\frac{1-2\upsilon}{2-2\upsilon}\left[A_{11} + B_{11} + 4A_1\right]\\
C_{22} &= -C_{11}\frac{1-2\upsilon}{9-10\upsilon}, \quad D_{22} = -D_{11}
\end{aligned}
\tag{47}
$$

### 8.3 Appendix 3

Evaluation of the constants in Eqs. (38) and (39) leads to:

$$
\begin{aligned}
a_2 &= \left[3A_{22} + \frac{\upsilon}{1-2\upsilon}\left(4A_{22} + 2C_{22} + \frac{1}{2}a_1\right)\right]\left[\frac{-2\left(\lambda^{10} - \lambda^2 + 1\right)}{\lambda^2\left(\lambda^4 - 1\right)\left(\lambda^4 - \lambda^2 + 4\right)}\right]\\
b_2 &= \frac{1}{6}\left[3A_{22} + \frac{\upsilon}{1-2\upsilon}\left(4A_{22} + 2C_{22} + \frac{1}{2}a_1\right)\right]\left[\frac{-2\lambda^{10} - \lambda^8 + 2\lambda^6 + 2\lambda^4 - 3}{\lambda^2\left(\lambda^4 - 1\right)\left(\lambda^4 - \lambda^2 + 4\right)}\right] - \frac{1}{6}\left[C_{22} - A_{22}\right]
\end{aligned}
$$

$$
\begin{aligned}
c_2 &= \frac{1}{3}\left[3A_{22}+\frac{\upsilon}{1-2\upsilon}\left(4A_{22}+2C_{22}+\frac{1}{2}a_1\right)\right]\left[1+\frac{2\left(1-\lambda^2-\lambda^4\right)}{\left(\lambda^4-1\right)\left(\lambda^4-\lambda^2+4\right)}\right]\\
d_2 &= \frac{1}{2}\left[3A_{22}+\frac{\upsilon}{1-2\upsilon}\left(4A_{22}+2C_{22}+\frac{1}{2}a_1\right)\right]\left[\frac{\lambda^6-1}{\lambda^2\left(\lambda^4-\lambda^2+4\right)}\right]\\
e_2 &= \frac{1}{2}\left[\left(\frac{4\upsilon^2-13\upsilon+4}{2-4\upsilon}\right)a_1+3D_{22}\right]\frac{1-\lambda}{1-\lambda^{-4}}\\
f_2 &= \frac{1}{2}\left[\left(\frac{4\upsilon^2-13\upsilon+4}{2-4\upsilon}\right)a_1+3D_{22}\right]\frac{\lambda\left(\lambda^{-5}-1\right)}{1-\lambda^{-4}}
\end{aligned}
\tag{48}
$$

## 8.4 Appendix 4

The coefficients appearing in Eq. (40) are given as follows:

$$
\begin{aligned}
L_5 &= \frac{-1}{1-2\upsilon}\left[3b_2\left(8\upsilon^2-6\upsilon+1\right)+\frac{1}{2}A_{22}\left(1-2\upsilon\right)-C_{22}\left(1+\upsilon\right)+\frac{3}{4}B_1+A_1\left(7\upsilon-\frac{23}{4}\right)-\frac{9}{4}a_1\left(3-4\upsilon\right)\right]\\
L_6 &= -d_2\\
L_7 &= \frac{1}{1-2\upsilon}\left[\frac{-3}{4}a_1\left(3-4\upsilon\right)+B_1\left(4\upsilon-1\right)+A_1\left(4\upsilon-5\right)-6b_2\left(\upsilon-1\right)+C_{22}\left(\upsilon+1\right)+A_{22}\left(\upsilon-1\right)\right]\\
L_8 &= \frac{1}{1-2\upsilon}\left[6c_2\left(1-\upsilon\right)\right],\quad L_9=\frac{-1}{1-2\upsilon}\left[d_2\left(-8\upsilon^2+6\upsilon+2\right)\right],\quad L_{10}=\frac{-1}{1-2\upsilon}\left[2a_2\left(1-\upsilon\right)\right]\\
L_{11} &= \frac{1}{1-2\upsilon}\left[\frac{-3}{4}a_1\left(3-4\upsilon\right)+\frac{1}{4}B_1\left(16\upsilon-5\right)+\frac{1}{4}A_1\left(4\upsilon-5\right)-2b_2\left(10\upsilon^2-20\upsilon+9\right)-C_{22}\left(3-5\upsilon\right)-A_{22}\upsilon+D_{22}\right]\\
L_{12} &= \frac{-1}{1-2\upsilon}\left[2d_2\left(1-\upsilon\right)\right],\quad L_{13}=\frac{1}{1-2\upsilon}e_2, L_{14}=\frac{1}{1-2\upsilon}f_2,\quad L_{15}=\frac{3}{2}e_2,\quad L_{16}=\frac{-1}{2}f_2\\
L_{17} &= \frac{1}{1-2\upsilon}\left[-D_{22}\left(1-2\upsilon\right)+\frac{3}{2}a_1\left(3-4\upsilon\right)-\frac{1}{2}A_1\left(3+4\upsilon\right)-\frac{1}{2}B_1\left(5-4\upsilon\right)+12b_2\left(1-2\upsilon\right)+4A_{22}+2C_{22}\right]\\
L_{18} &= \frac{1}{1-2\upsilon}\left[4d_2\left(1-2\upsilon\right)\right],\quad L_{19}=\frac{-3}{2}f_2\\
L_{20} &= \frac{1}{1-2\upsilon}\left[-2D_2\left(1-2\upsilon\right)+\frac{3}{4}a_1\left(3-4\upsilon\right)-\frac{1}{2}A_1\left(3+4\upsilon\right)+\frac{1}{2}B_1\left(1-4\upsilon\right)\right]
\end{aligned}
\tag{49}
$$

The coefficients appearing in Eq. (42) are given as:

$$
\begin{aligned}
H_1\left(\varsigma\right) &= \left[\frac{4L_{21}-3\upsilon\left(L_{21}-L_{24}\right)}{1-2\upsilon}\varsigma^3+\frac{3\upsilon\left(L_{22}+L_{25}\right)-2L_{22}}{1-2\upsilon}\varsigma^{-3}+\frac{\upsilon\left(L_{23}+3L_{26}\right)}{1-2\upsilon}\varsigma^{-1}\right]\\
&\quad+\left[b_2\left(3-4\upsilon\right)\varsigma^3+c_2\varsigma^{-3}-d_2\varsigma^{-1}+\frac{1}{2}A_{22}\varsigma^3+\frac{1}{2}C_{22}\varsigma^3+\frac{1}{4}\left(B_1-A_1\right)\varsigma^3-a_1\varsigma^3\right]\\
H_2\left(\varsigma\right) &= \frac{-1}{2}\left[3\left(L_{21}-L_{24}\right)\varsigma^3+3\left(L_{22}+L_{25}\right)\varsigma^{-3}+\left(3L_{23}+L_{26}\right)\varsigma^{-1}\right]\\
H_3\left(\varsigma\right) &= -\frac{1}{8}\left[-L_{18}\varsigma^{-2}+3L_{16}\varsigma^2+4L_{17}\varsigma^3\right]-\frac{1}{4}\left[e_2\varsigma^{-2}+f_2\varsigma^2+D_{22}\varsigma^3\right]+\frac{1}{4}A_1\varsigma^3\\
&\quad-\frac{1}{2}\left[a_2\varsigma+b_2\left(-4\upsilon\right)\varsigma^3-c_2\varsigma^{-3}+d_2\left(4\upsilon-4\right)\varsigma^{-1}+A_{22}\varsigma^3\right]+\frac{1}{4}a_1\varsigma^3
\end{aligned}
\tag{50}
$$

and

$$
\begin{aligned}
L_{21} &= \frac{-1}{20\upsilon-11}L_1,\quad L_{24}=\frac{1}{20\upsilon-19}L_7,\quad L_{22}=\frac{1}{20\upsilon-11}L_2,\\
L_{25} &= \frac{1}{20\upsilon-19}L_8,\quad L_{23}=\frac{-1}{20\upsilon-11}L_3,\quad L_{26}=\frac{-1}{20\upsilon-19}L_9
\end{aligned}
\tag{51}
$$

### 8.5 Appendix 5

Evaluation of the constants in Eqs. (41) and (42) leads to:

$$
\begin{aligned}
&a_3 = 4c_3 - 9d_3 - \frac{1}{4}\left(H_2(1) + 2H_1(1)\right), \quad b_3 = c_3 - 2d_3 - \frac{1}{8}\left(H_2(1) + H_1(1)\right)\\
&c_3 = \frac{X_3X_5 - X_6X_2}{X_1X_5 - X_4X_2}, \quad e_3 = \frac{\frac{2}{3}\left[H_3(\lambda) - \lambda^2 H_3(1)\right]}{\lambda^2 - \lambda^{-4}}\\
&d_3 = \frac{X_6X_1 - X_3X_4}{X_1X_5 - X_4X_2}, \quad f_3 = \frac{\frac{2}{3}\left[H_3(\lambda) - \lambda^{-4} H_3(1)\right]}{\lambda^2 - \lambda^{-4}}
\end{aligned}
\tag{52}
$$

where

$$
\begin{aligned}
&X_1 = 8\lambda - 4\lambda^{-3} - 4\lambda^{-5}, \quad X_4 = -8\lambda + 12\lambda^3 - 4\lambda^{-5}\\
&X_2 = -18\lambda + 8\lambda^3, \quad X_6 = 18\lambda - 24\lambda^3 + 6\lambda^{-3}\\
&X_3 = -H_1(\lambda) + \frac{1}{2}\left[H_2(1) + 2H_1(1)\right]\lambda - \frac{1}{2}\left[H_2(1) + H_1(1)\right]\lambda^3\\
&X_6 = -H_2(\lambda) - \frac{1}{2}\left[H_2(1) + 2H_1(1)\right]\lambda + \frac{3}{2}\left[H_2(1) + H_1(1)\right]\lambda^3
\end{aligned}
\tag{53}
$$

## References


1. Asadi, H., Akbarzadeh, A.H., Chen, Z.T., Aghdam, M.M.: Enhanced thermal stability of functionally graded sandwich cylindrical shells by shape memory alloys. Smart Mater. Struct. **24**(4), 045022 (2015)
2. Akbarzadeh, A., Chen, Z.: Thermo-magneto-electro-elastic responses of rotating hollow cylinders. Mech. Adv. Mater. Struct. **21**(1), 67–80 (2014)
3. Von Karman, T.: Uber die Formanderung Dunnwandiger Rohre, insbesondere federnder Ausgleichsrochre. VDI-Zeitdchriff **55**, 1889–1895 (1911)
4. Brazier, L.G.: On the flexure of thin cylindrical shells and other thin sections. Proc. R. Soc. Lond. A **116**(773), 104–114 (1927)
5. Ting, T.C.T.: Pressuring, shearing, torsion and extension of a circular tube or bar of cylindrically anisotropic material. Proc. R. Soc. Lond. A **452**, 2397–2421 (1996)
6. Ting, T.C.T.: New solution to pressuring, shearing, torsion and extension of cylindrically anisotropic elastic circular tube or bar. Proc. R. Soc. Lond. A **455**, 3527–3542 (1999)
7. Chen, T., Chung, C.T., Lin, W.L.: A revisit of a cylindrically anisotropic tube subjected to pressuring, shearing, torsion and extension and a uniform temperature change. Int. J. Solids Struct. **37**, 5143–5159 (2000)
8. Boyle, J.T.: The finite bending of curved pipes. Int. J. Solids Struct. **17**, 515–529 (1981)
9. Reissner, E.: On finite pure bending of curved tubes. Int. J. Solids Struct. **17**(9), 839–844 (1981)
10. Emmerling, F.A.: Flexible Shells. Springer, Berlin (1984)
11. Lang, H.A.: The theory of toroidal elasticity. Res Mech. Int. J. Struct. Mech. Mater. Sci. **26**(4), 289–351 (1989)
12. Gohner, O.: Schubspannungsverteilung im Querschnitt einer Schraubenfeder. Ing. Arch. **1**, 619–664 (1930)
13. Ancker, C.J., Goodier, J.N.: Pitch and curvature corrections for helical springs. 58-APM, ASME (1958)
14. Kornecki, A.: Stress distribution in a pressurized thick-walled toroidal shell—a three dimensional analysis. College of Aeronautics, Cranfield, England, Note 137 (1963)
15. McGill, D.J., Rapp, I.H.: Axisymmetric stresses and displacements in thick-walled elastic torus. J. Eng. Mech. Div. **99**(3), 629–633 (1973)
16. Redekop, D.: A displacement solution in toroidal elasticity. Int. J. Press. Vessels Pip. **51**, 1–21 (1992)
17. Zhu, Y., Redekop, D.: An out-of-plane displacement solution in toroidal elasticity. Int. J. Press. Vessels Pip. **58**(3), 309–319 (1994)
18. Eric, R.: On finite bending of pressurized tubes. Trans. ASME **26**, 386–392 (1959)
19. Madureira, L.R., Melo, F.Q.: Hybrid formulation solution for stress analysis of curved pipes with welded bending joints. Eng. Fract. Mech. **77**(15), 2992–2999 (2010)
20. Fonseca, E.M.M., de Melo, F.J.M.Q.: Numerical solution of curved pipes submitted to in-plane loading conditions. Thin Walled Struct. **48**(2), 103–109 (2010)
21. Kolesnikov, A.M.: Large bending deformations of pressurized curved tubes. Arch. Mech. **63**(5–6), 507–516 (2011)
22. Christo Michael, T., Veerappan, A.R., Shanmugam, S.: Effect of ovality and variable wall thickness on collapse loads in pipe bends subjected to in-plane bending closing moment. Eng. Fract. Mech. **79**, 138–148 (2012)
23. Zhu, Y., Luo, X.Y., Wang, H.M., Ogden, R.W., Berry, C.: Three-dimensional non-linear buckling of thick-walled elastic tubes under pressure. Int. J. Non-Linear Mech. **48**, 1–14 (2013)
24. Levyakov, S.V.: Evaluation of Reissner's equations of finite pure bending of curved elastic tubes. J. Appl. Mech. **81**(4), 1–9 (2013)
25. Yudo, H., Yoshikawa, T.: Buckling phenomenon for straight and curved pipe under pure bending. J. Mar. Sci. Technol. **20**(1), 94–103 (2014)

26. Alashti, R.A., Ahmadi, S.A.: Buckling of imperfect thick cylindrical shells and curved panels with different boundary conditions under external pressure. J. Theor. Appl. Mech. **52**(1), 25–36 (2014)
27. Hamdaoui, M.E.I., Merodio, J., Ogden, R.W., Rodríguez, J.: Finite elastic deformations of transversely isotropic circular cylindrical tubes. Int. J. Solids Struct. **51**(5), 1188–1196 (2014)
28. Djamaluddin, F., Abdullah, S., Ariffin, A.K., Nopiah, Z.M.: Non-linear finite element analysis of bitubal circular tubes for progressive and bending collapses. Int. J. Mech. Sci. **99**, 228–236 (2015)
29. Rodríguez, J., Merodio, J.: Helical buckling and post buckling of pre-stressed cylindrical tubes under finite torsion. Finite Elem. Anal. Des. **112**, 1–10 (2016)
30. Yazdani Sarvestani, H., Hoa, S.V., Hojjati, M.: Three-dimensional stress analysis of orthotropic curved tubes-part 1: single-layer solution. Eur. J. Mech. A Solids **60**, 327–338 (2016)
31. Yazdani Sarvestani, H., Hojjati, M.: Three-dimensional stress analysis of orthotropic curved tubes-part 2: laminate solution. Eur. J. Mech. A Solids **60**, 339–358 (2016)
32. Yazdani Sarvestani, H., Hojjati, M.: Failure analysis of thick composite curved tubes. Compos. Struct. **160**, 1027–1041 (2017)